Supplementary Information for: Towards MRI axon radius mapping in clinical settings: insights from MRI-scale histology and experimental validation

Laurin Mordhorst[1,2*], Luke J. Edwards[3], Maria Morozova[3,4], Mohammad Ashtarayeh[2], Tobias Streubel[2], Björn Fricke[1,2], Francisco J. Fritz[2], Henriette Rusch[4], Carsten Jäger[3,4], Ludger Starke[5], Thomas Gladytz[5], Ehsan Tasbihi[5,6], Joao S. Periquito[5], Andreas Pohlmann[5], Thoralf Niendorf[5,6], Nikolaus Weiskopf[3,7,8], Markus Morawski[3,4], Siawoosh Mohammadi[1,2,9*]

[1]Department, University Hospital of Luebeck, Luebeck, Germany.
[2]Institute of Systems Neuroscience, University Medical Center Hamburg-Eppendorf, Hamburg, Germany.
[3]Department of Neurophysics, Max Planck Institute for Human Cognitive and Brain Sciences, Leipzig, Germany.
[4]Paul Flechsig Institute - Centre of Neuropathology and Brain Research, Medical Faculty, Leipzig University, Leipzig, Germany.
[5]Berlin Ultrahigh Field Facility (B.U.F.F.), Max Delbrück Center for Molecular Medicine in the Helmholtz Association, Berlin, Germany.
[6]Charité – Universitätsmedizin Berlin, Berlin, Germany.
[7]Felix Bloch Institute for Solid State Physics, Leipzig University, Leipzig, Germany.
[8]Wellcome Centre for Human Neuroimaging, Institute of Neurology, University College London, London, United Kingdom.
[9]Max Planck Research Group MRI Physics, Max Planck Institute for Human Development, Berlin, Germany.

Contributing authors: laurin.mordhorst@uni-luebeck.de; siawoosh.mohammadi@uni-luebeck.de;

SI1 Axon radius distributions from light microscopy

Fig. S1 shows axon radius distributions from our two histological tissue samples for five regions of the corpus callosum: genu, anterior midbody, midbody, posterior midbody, and splenium. Axon radius distributions and r_{eff} are similar across tissue samples (see Fig. S1c-f), except for the genu (see Fig. S1b). Yet, tissue sample CC-02 generally exhibits slightly higher r_{eff} than CC-01. The pattern of r_{eff} across anterior midbody, midbody, posterior midbody, and splenium (see Fig. S1c-f) follows an alternating low-high pattern.

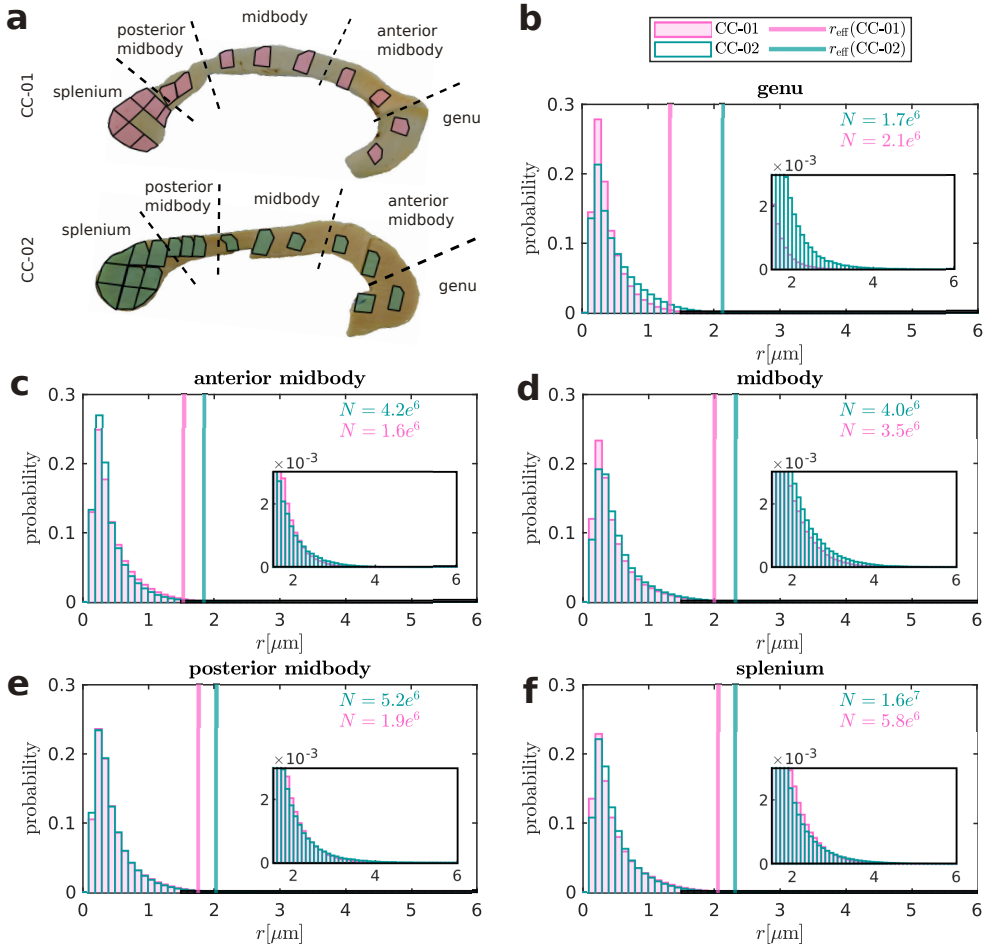

Fig. S1 Axon radius distributions from light microscopy. **(a)** Corpus callosum sketch with light microscopy ROIs (polygons) and segmentation into five regions (dashed lines). **(b-f)** Axon radius distributions pooled over the light microscopy ROIs for each corpus callosum region shown in (a). Colors indicate tissue sample (see legend in (b)). Vertical lines denote r_{eff} as per Eq. (1). Annotated numbers inside the plot denote axon count. Insets highlight the tail of axon radius distributions.

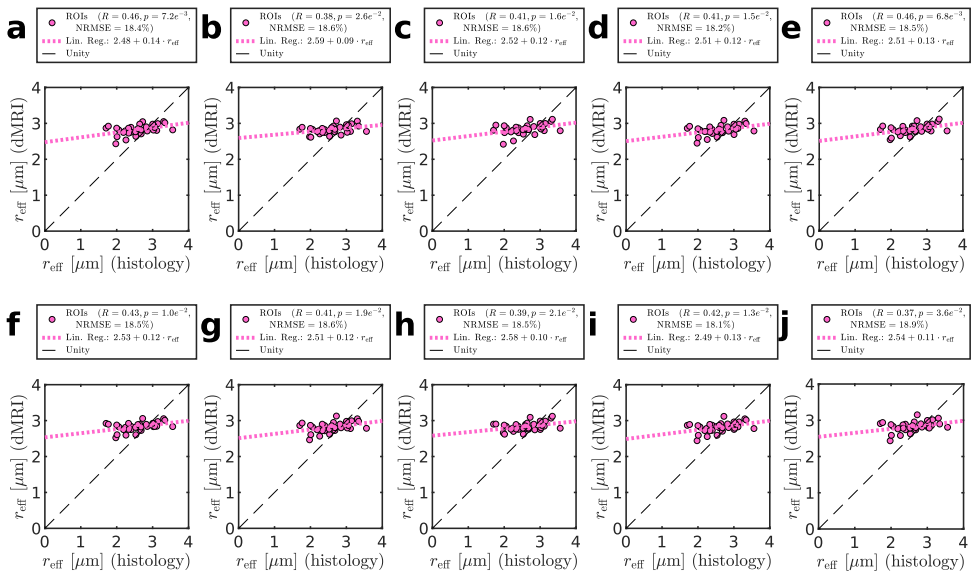

Fig. S2 Reproducibility of correlation between in-vivo dMRI-based r_{eff} and histological r_{eff}. (a-j) Quantitative comparisons of r_{eff} from in-vivo dMRI against histology. Each plot represent one of ten repeated runs through our in-vivo processing pipeline. Markers represent histological ROIs from Fig. 1a, with in-vivo dMRI-based r_{eff} reflecting the group-average. The dashed lines illustrate theoretical perfect agreement. The legends provide metrics computed over all ROIs, including Pearson's correlation coefficient (R) with corresponding p-value, and the normalized root-mean-square error (NRMSE) (see Section 4.7 for metric definitions).

SI2 Reproducibility of correlation between in-vivo dMRI-based r_{eff} and histological r_{eff}

In-vivo dMRI-based r_{eff} exhibited some variability due to the non-deterministic nature of our processing pipeline (see Section 4.4). To assess the impact of this variability on correlation, we repeated the quantitative analysis in Fig. 2k for ten separate runs of the pipeline.

Qualitatively, comparison group-average r_{eff} from in-vivo dMRI show a consistent trend across all iterations. Pearson's R varied between 0.37 ($p = 3.6e^{-2}$, see Fig. S2j) to 0.46 ($p \approx 7e-3$, see Fig. S2a,e), with a mean of $R = 0.414 \pm 0.03$. All correlations were statistically significant ($p < 0.05$).

SI3 Per-subject analyses for in-vivo dMRI-based r_{eff}

While Fig. 2i,l in the main manuscript presents group-average r_{eff} for our in-vivo dMRI experiments, here we show per-subject results, including both spatial patterns across the corpus callosum (see Fig. S3a-e) and quantitative comparisons with histology (see Fig. S3f-j).

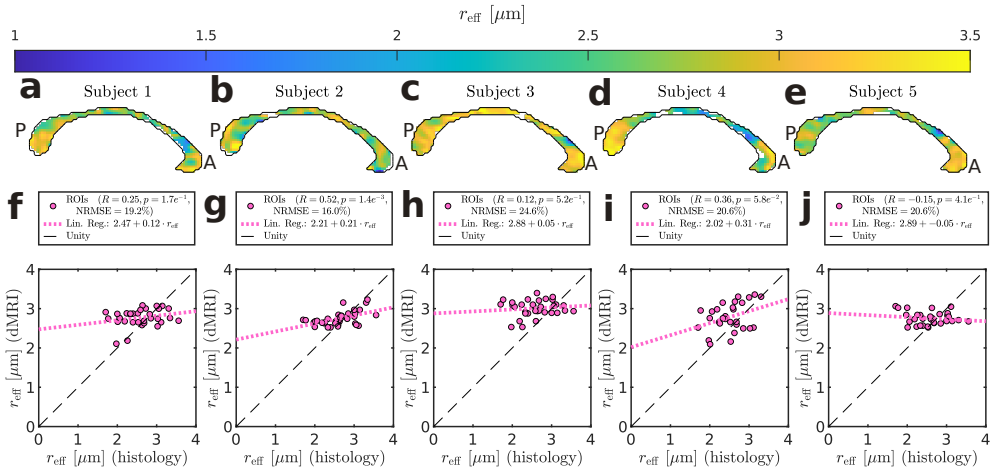

Fig. S3 Per-subject analyses for in-vivo dMRI-based r_{eff} (a-e) Per-subject spatial patterns of r_{eff} across the corpus callosum, shown in mid-sagittal section of MNI space. **(f-j)** Per-subject quantitative comparison of in-vivo dMRI-based r_{eff} against histology. Markers represent histological ROIs in Fig. 1a. The dashed lines illustrate theoretical perfect agreement. The legends provide metrics computed over all ROIs, including Pearson's correlation coefficient (R) and the corresponding p-value, the normalized root-mean-square error (NRMSE) (see Section 4.7 for metric definitions).

The spatial r_{eff} patterns are consistent across subjects in showing higher values in the genu and splenium and lower values in the anterior midbody. However, overall, inter-subject variability appears to be substantial. This variability is also reflected in the quantitative comparisons with histology: while r_{eff} generally increases with histological values for most subjects (see Fig. 2f-i), there's a significant correlation with histology only for one subject (see Fig. 2g).

SI4 Impact of f_{im} on ex-vivo dMRI-based r_{eff}

Ex-vivo dMRI-based r_{eff} estimation relies on estimating of f_{im} (see Section 4.3 for our approach). Fig. S4 illustrates how this estimation affects r_{eff}, showing both spatial patterns (see Fig. S4a-b) and the relationship between r_{eff} and f_{im} (see Fig. S4c).

The spatial pattern of r_{eff} suggest a relationship with f_{im}. This relationship is particularly evident in the splenium, where sampling density is highest. The quantitative comparison in Fig. S4c further supports this by showing that r_{eff} scales approximately linearly with f_{im} in the splenium. These findings indicate that f_{im} is a confounding factor in r_{eff} estimation, at least for our f_{im} estimation approach.

SI5 Scaling behavior of the model-inherent bias across broader r_{eff} ranges

The simulations in Fig. 2n suggest that the model-inherent bias of r_{eff} in dMRI scales proportionally with histological r_{eff}. To investigate this scaling behavior across

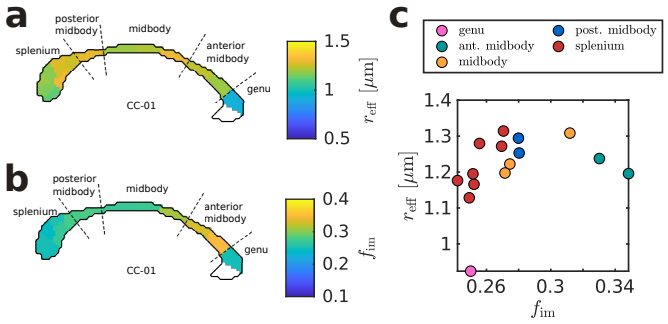

Fig. S4 Impact of f_{im} on ex-vivo dMRI-based r_{eff} (a) Spatial patterns of ex-vivo dMRI-based r_{eff} across the corpus callosum, shown in mid-sagittal MNI slice with subregions indicated (dashed lines). Spatial patterns were interpolated using the nearest-neighbor method, evaluated at the ROI locations in Fig. 1a. The void in the genu indicates a ROI not scanned with ex-vivo dMRI (see Fig. 5e). **(b)** Corresponding spatial pattern of f_{im}. **(c)** Relationship between f_{im} and r_{eff}. Each marker represents one ROI from Fig. 1a, with marker colors indicating corpus callosum subregions as defined by dashed lines in (a-b).

a broader range of histological r_{eff} values, we extended simulations to mimic different axon populations beyond the corpus callosum. Fig. S5a illustrates this approach: Using our histological axon radius distributions of the corpus callosum as a primary dataset, we scaled axon radii to extrapolate axon radius distributions of the rat corpus calllosum (scaling factor: 0.5 [14]) and the human corticospinal tract (scaling factor: 1.15 [5]). For in-vivo simulations, these scaling factors were applied alongside the tissue shrinkage compensation factor (1.3). For example, we used the scaling factor $1.15 \cdot 1.3 \approx 1.5$ for in-vivo corticospinal tract simulations.

Fig. S5b-f show comparisons of r_{eff} from dMRI simulations against histological values across all ROIs. Generally, the model-inherent bias causes strong deviations from the unity line for large r_{eff}, resulting in a reduced dynamic range as indicated by the slopes of linear regressions. Notably, the model-inherent bias scales non-linearly with r_{eff}, showing a tendency toward saturation at large r_{eff}. Additionally, the model-inherent bias also scales with g_{max} (see titles of Fig. S5b-f), resulting in very strong deviations for in-vivo next-generation research scanners or ex-vivo preclinical scanners (see Fig. S5e-f).

SI6 The origins of the model-inherent bias

The simulations in Fig. 2m reveal a model-inherent bias of dMRI-based r_{eff}. Here, we investigate the origins of this bias by assessing the signal approximations involved in deriving r_{eff} (see Section A). These approximations, applied in sequence, include:

- the Gaussian phase approximation (GPA; see Eq. (A5)),
- the wide pulse approximation (WPA; see Eq. (A6)),
- the Taylor approximation (see Eq. (A9)),
- the exponential approximation (see Eq. (A10)).

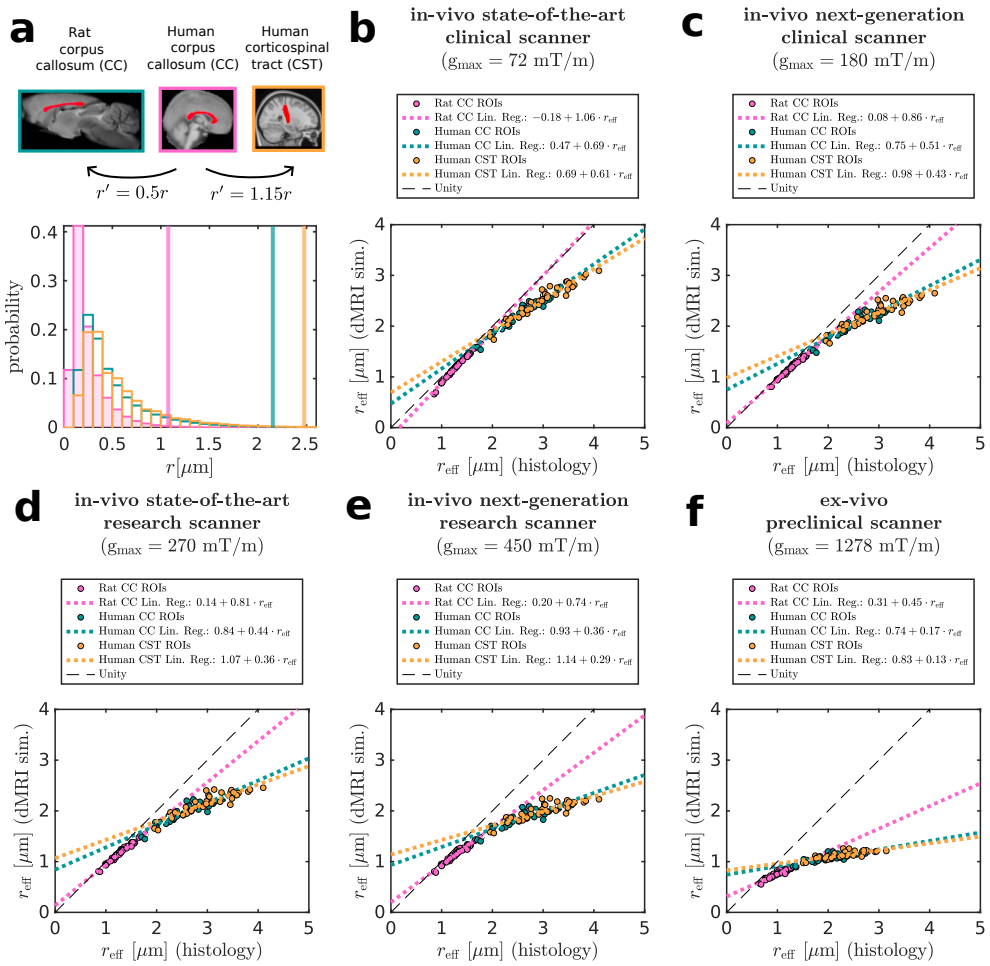

Fig. S5 Scaling behavior of the model-inherent bias across broader r_{eff} ranges. (a) Axon radius distributions for different populations: rat corpus callosum (green), human corpus callosum (magenta), and human corticospinal tract (orange). Vertical lines indicate r_{eff} values computed from these distributions. The human corpus callosum data is the primary dataset, whereas the other axon populations were extrapolated by scaling each radius from human corpus callosum distributions as annotated (see arrows). Distributions reflect the ex-vivo scenario, whereas for in-vivo simulations, we accounted for tissue shrinkage by scaling with an additional factor of 1.3 [31, 38]. textbf(b-f) Comparison of r_{eff} from idealized dMRI simulations (SNR = ∞) against histological r_{eff} for: optimal in-vivo protocols determined in Fig. 3 (corresponding to markers for "SNR baseline level: reference") and **(e)** our experimental ex-vivo protocol. Marker/line colors indicate axon population as in (a). Dashed lines illustrate theoretical perfect agreement; dotted lines are linear regressions per axon population. The full set of protocol parameters is given in Table S1 for in-vivo protocols (see table rows with $\eta = 1.3$), whereas the ex-vivo protocol is described in Section 4.3.

We evaluated the accuracy of these approximations at the level of the powder-averaged signal $S^\circ(b, H(r))$ (see Eq. (A7)) – the signal to which r_{eff} is fitted. While the Taylor approximation and exponential approximation directly model $S^\circ(b, H(r)) \approx S^\circ(b, r_{\text{eff}})$, the matrix method, the GPA and the WPA model signals per gradient direction $S(b, \vec{g}, H(r))$ as per Eq. (A1). For the latter methods, we first simulated $S(b, \vec{g}, H(r))$ and then estimated $S^\circ(b, H(r))$ using a Gaussian maximum likelihood estimator.

Fig. S6 shows $S^\circ(b, H(r))$ simulated using each of these approaches for both the optimal in-vivo dMRI protocols for different scanners identified in Fig. 3 and our experimental ex-vivo dMRI protocol.

The Taylor approximation drives the model-inherent bias

The Taylor approximation introduces the largest deviations between successive approximations, while the WPA results in smaller but noticeable deviations, and the GPA causes almost none. Notably, for both Taylor approximation and WPA, deviations increase for protocols with high g_{max} and are generally less pronounced for $S^\circ(b_{\text{min}}, H(r))$ (see Fig. S6a-e) compared to $S^\circ(b_{\text{max}}, H(r))$ (see Fig. S6f-j).

The dependency of the model-inherent bias on r_{eff} and g_{max}

The observed scaling of deviations with r_{eff} and g_{max} for the Taylor approximation and the WPA can be understood by examining their underlying dependencies. For the Taylor approximation, accuracy improves when the necessary but not sufficient condition $\kappa r_{\text{eff}}^4 \ll 1$ is satisfied. While the violation of this condition with increasing r_{eff} is evident, its violation with increasing g is implicit in the quadratic dependency $g^2 \sim \kappa = \frac{7}{48}\frac{g^2\gamma^2\delta}{D_0}$. Similarly, the deviations caused by the WPA ($\delta >> r^2/D_0$) are related to both r_{eff} and g_{max}. Higher r_{eff} are linked to the prevalence of larger r, making the assumption less valid, while higher g_{max} typically allow for shorter δ, further undermining the assumption. In ex-vivo dMRI, the reduced D_0 further amplifies the deviations due to both Taylor approximation and WPA.

Powder-averaged signals decay near-linearly for high g_{max}

Interestingly, $S^\circ(b, H(r))$ appears to decay almost linearly with r_{eff} for protocols with high g_{max}. This behavior suggests an intrinsic property of the signal model, warranting further exploration.

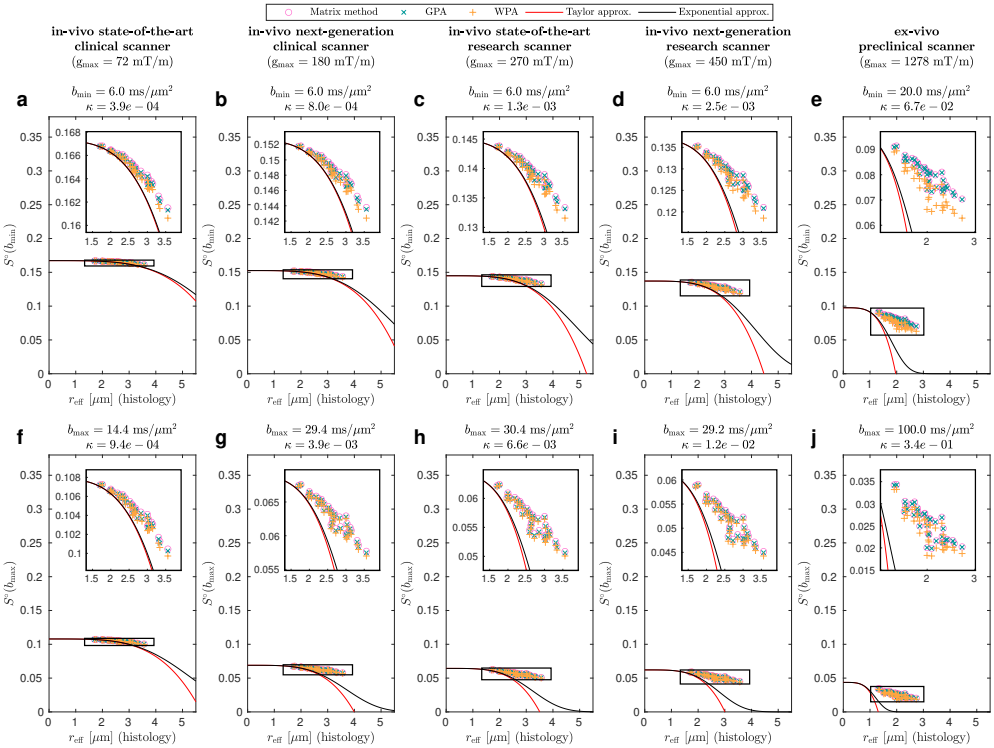

Fig. S6 The origins of the model-inherent bias. **(a-e)** Simulated powder-averaged signals $S^{\circ}(b_{\text{min}})$ for the lowest b-shell of the protocol with $b = b_{\text{min}}$. Columns indicate different scanners/protocols with varying maximum gradient amplitude g_{max} (see titles): **(a-d)** optimal in-vivo protocols determined in Fig. 3 (corresponding to markers for "SNR baseline level: reference") and **(e)** our experimental ex-vivo protocol. Marker symbols/lines denote different methods to simulate $S^{\circ}(b_{\text{min}})$, arranged in order of successive simplifications during derivation of r_{eff} from left to right in the legend. Distinct markers reflect simulations for ROIs in Fig. 1a, whereas lines reflect $S^{\circ}(b)$ signal models. The κ values, annotated above plots, are protocol-specific factors used in the wide pulse approximation (WPA; see Eq. (A6)). The b_{min} values were chosen to suppress extra-axonal signal and depend only on experimental conditions (in-vivo vs. ex-vivo, see annotation above plots). **(f-j)** Simulated $S^{\circ}(b_{\text{max}})$ for the highest b-shell of the protocol with $b = b_{\text{max}}$, with definitions as in (a-e). The b_{max} values vary across protocols (see annotation above plots). The full set of protocol parameters is given in Table S1 for in-vivo protocols (see rows with $\eta = 1.3$), whereas the ex-vivo protocol is described in Section 4.3.

SI7 dMRI protocol optimization (additional results)

We optimized in-vivo dMRI protocols in Section 2.3 assuming a radius scaling factor $\eta = 1.3$ for tissue shrinkage compensation [31, 38]. Here we repeated in-vivo protocol optimization for $\eta = 1.0$ and $\eta = 1.5$, representing more extreme scenarios of no tissue shrinkage and very strong tissue shrinkage. As in Section 2.3, we conducted the protocol optimization analyses with increased baseline SNR levels to study the potential impact of technical or acquisition improvements.

Fig. S7 shows R and NRMSE as a function of $g_{\max}$ for different η. For any η, R curves show similar qualitative behavior, converging to a maximum R for a certain $g_{\max}$ (see Fig. S7a-c), roughly coinciding with optimal NRMSE (see Fig. S7d-f). Yet, for $\eta = 1$, this $g_{\max}$ is outside the range of values of exisiting in-vivo scanners at reference SNR baseline level (see Fig. S7a). For $\eta \geq 1.3$ optimal R can be achieved with existing scanners (see Fig. S7b-c), with NRMSE becoming suboptimal (larger) for higher $g_{\max}$ (see Fig. S7e-f).

Fig. S8 shows comparisons of simulated r_{eff} estimates against histological values for the optimal protocols across different scanners, complementing the metrics shown in Fig. S7. These plots illustrate that R and NRMSE are determined by precision rather than bias for small η and $g_{\max}$. Yet, at large η and $g_{\max}$, the model-inherent bias strongly reduces the sensitivity to large axons, leading to the non-optimal NRMSE at high $g_{\max}$ values observed in Fig. S7e-f.

Table S1 show the optimal parameters for protocols presented in Figs. S7 and S8. The parameters for $\eta = 1.3$ correspond to the optimal parameters shown in the main manuscript (see Section 2.3).

SI8 Influence of Gaussian and Rician noise on r_{eff} estimation

We used Rician-distributed magnitude dMRI for our experimental validation of r_{eff}, shown in Fig. 2k. To mimic these conditions, we also incorporated Rician noise into our dMRI simulations (see Fig. 2l). For comparison, we replicated these simulations using Gaussian noise to assess the potential improvements achievable with Gaussian-distributed signals, assuming such distributions can be achieved through advanced preprocessing techniques [16, 39, 41].

Fig. S9a-b compare the impact of Gaussian and Rician noise on r_{eff} from dMRI simulations against histological r_{eff}, both for the ex-vivo and in-vivo scenario. In ex-vivo dMRI simulations (see Fig. S9a), the noise distribution has little impact, likely due to the large number of diffusion measurements (585 directions across shells). In-vivo (see Fig. S9b), Gaussian noise allows for better precision than Rician noise, translating into improved R and NRMSE. It should be noted that the impact of Rician noise on r_{eff} estimates is likely underestimated here, as the noise level σ was assumed to be known in our simulations. In practice, σ is typically unknown and must be estimated. This σ-estimation, likely imperfect, can be expected to propagate additional errors into r_{eff}.

SI9 Impact of spatial smoothing on in-vivo dMRI-based r_{eff}

In the main manuscript, we applied spatial smoothing to in-vivo dMRI-based r_{eff} maps prior to comparison with histological values (see Fig. 2h,l). In Fig. S10, we illustrate the impact of spatial smoothing on r_{eff}, including both a spatial r_{eff} pattern for an exemplary subject in native space (see Fig. S10a-b) and its effect on the quantitative comparison with histology for the group-average r_{eff} (see Fig. S10c-d).

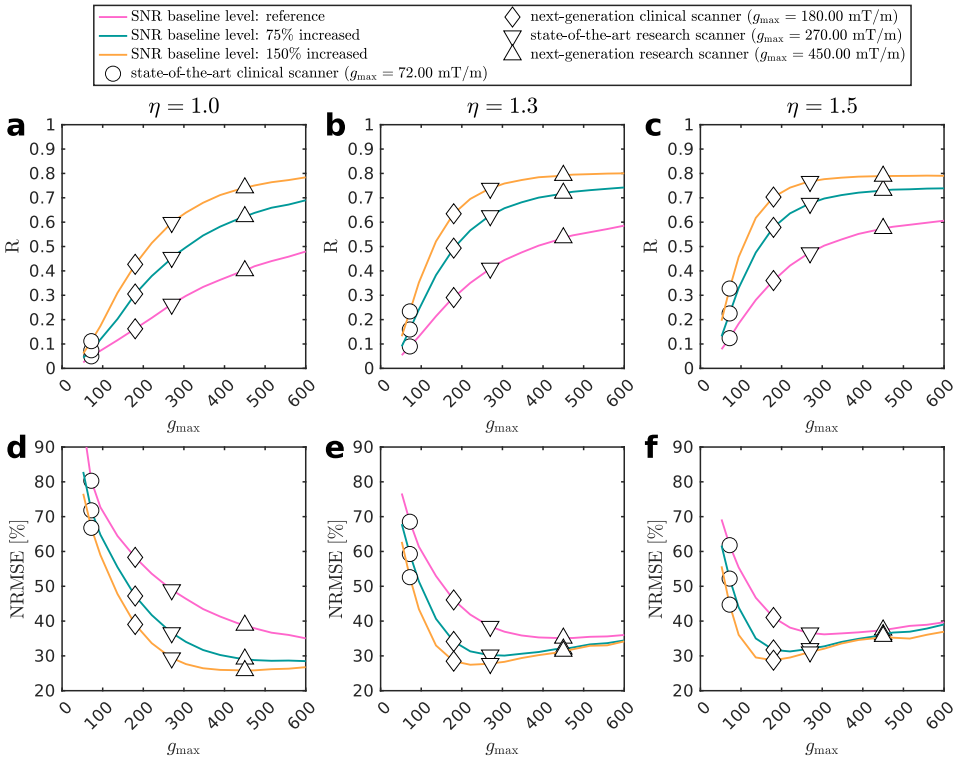

Fig. S7 Optimal in-vivo protocol metrics for different axon radius scaling factors. (a-c) Optimal Pearson's correlation coefficients (R) as a function of maximum gradient amplitude (g_{max}). Columns show R for different radius scaling factors used to compensate for tissue shrinkage: **(a)** $\eta = 1$, **(b)** $\eta = 1.3$ and **(c)** $\eta = 1.5$. While $\eta = 1.3$ [31, 38] was used as an estimate for in-vivo conditions in the main manuscript, $\eta = 1.0$ and $\eta = 1.5$ represent the scenarios of no tissue shrinkage and very strong tissue shrinkage. Markers encode g_{max} of existing clinical scanners and research scanners (assuming 90 % of the nominal g_{max}). Line colors indicate different SNR baseline levels. While the reference SNR baseline level reflects our experimental conditions, increased SNR baseline levels assume an SNR increase through potential technical or acquisition advances. In addition, the SNR of a particular protocol candidate depends on the protocol parameters (see Eq. (13)). For our experimental protocol, baseline SNR levels would correspond to SNR values of 32 (reference), 56 (75 % increased) and 80 (150 % increased). **(d-f)** Optimal normalized root-mean-square error (NRMSE) as a function of maximum gradient amplitude (g_{max}) for different η, with definitions as in (a-c). Note that we optimized protocols by minimizing R, whereas NRMSE is an auxiliary metric.

Smoothing preserves the overall spatial pattern, maintaining the high-low trend across the genu, anterior midbody, midbody, posterior midbody, and splenium (see Fig. S10a-b). However, it reduces local variations, making the pattern less sensitive to noise but potentially also to finer structural details. The quantitative comparison with histology in Fig. S10c-d confirms that smoothing is necessary to reveal a significant correlation. Importantly, smoothing appears to enhance precision without introducing spurious correlations.

Table S1 Parameters of optimal in-vivo dMRI protocols. All dMRI protocols use two shells with $\{60, 120\}$ diffusion gradient directions. The SNR baseline level describes the SNR conditions compared to our dMRI experiments. While the reference SNR baseline level corresponds to our experimental conditions, increased SNR baseline levels assume an SNR increase through potential technical or acquisition advances. η is a radius scaling factor compensating for tissue shrinkage in histology data, where $\eta = 1.3$ reflects the value assumed in the main manuscript. g_{min} and g_{max} are the diffusion gradient amplitudes of the two diffusion shells; $b_{\text{min}} = 6\,\text{ms}/\mu\text{m}^2$ and b_{max} denote the corresponding diffusion-weightings. δ and Δ are the gradient diffusion time and separation, consistent across shells. Echo time (T_{E}) was estimated according to Eq. (11). The SNR was estimated using Eq. (13), reflecting not only the baseline SNR level, but also protocol parameter-dependent SNR variation. Pearson's correlation coefficient (R) and its associated p-value, as well as the normalized root-mean square-error (NRMSE), and the fitting success rate (S) were computed as described in Section 4.7. The optimal dMRI protocol with maximum R per combination of η and SNR baseline level is highlighted in bold.

SNR baseline	η	g_{max} [mT/m]	g_{min} [mT/m]	b_{max} [ms/µm^2]	δ [ms]	Δ [ms]	T_{E} [ms]	SNR	R	p	NRMSE [%]	S [%]
reference	1.0	72	30.9	32.5	48	54	124	12.8	0.05	$8.4e^{-1}$	80.3	54.2
		180	81.3	29.4	24	30	76	27.3	0.16	$4.5e^{-1}$	58.3	68.7
		270	119.9	30.4	18	24	64	33.2	0.26	$1.8e^{-1}$	49.0	78.4
		450	**167.0**	**43.6**	**14**	**20**	**56**	**38.0**	**0.40**	$2.5e^{-2}$	**38.8**	**89.6**
	1.3	72	46.4	14.4	36	42	100	18.6	0.09	$7.0e^{-1}$	68.5	59.2
		180	81.3	29.4	24	30	76	27.3	0.29	$1.3e^{-1}$	46.1	82.5
		270	119.9	30.4	18	24	64	33.2	0.41	$2.0e^{-2}$	38.5	91.4
		450	**203.9**	**29.2**	**12**	**18**	**52**	**40.7**	**0.54**	$< 1e^{-3}$	**35.1**	**97.5**
	1.5	72	40.1	19.4	40	46	108	16.4	0.12	$5.8e^{-1}$	61.8	65.3
		180	81.3	29.4	24	30	76	27.3	0.36	$4.6e^{-2}$	41.0	89.4
		270	119.9	30.4	18	24	64	33.2	0.47	$4.8e^{-3}$	36.6	96.0
		450	**203.9**	**29.2**	**12**	**18**	**52**	**40.7**	**0.57**	$< 1e^{-3}$	**37.4**	**99.2**
75% increased	1.0	72	35.0	25.4	44	50	116	25.3	0.07	$7.6e^{-1}$	71.8	57.9
		180	81.3	29.4	24	30	76	47.7	0.31	$1.2e^{-1}$	47.2	79.3
		270	119.9	30.4	18	24	64	58.1	0.46	$9.9e^{-3}$	36.6	89.1
		450	**203.9**	**29.2**	**12**	**18**	**52**	**71.1**	**0.62**	$< 1e^{-3}$	**29.1**	**96.6**
	1.3	72	35.0	25.4	44	50	116	25.3	0.16	$4.6e^{-1}$	59.3	67.7
		180	81.3	29.4	24	30	76	47.7	0.49	$3.7e^{-3}$	34.1	92.7
		270	119.9	30.4	18	24	64	58.1	0.63	$< 1e^{-3}$	30.2	97.6
		450	**203.9**	**29.2**	**12**	**18**	**52**	**71.1**	**0.72**	$< 1e^{-3}$	**32.0**	**99.7**
	1.5	72	40.1	19.4	40	46	108	28.7	0.23	$2.7e^{-1}$	52.2	75.1
		180	81.3	29.4	24	30	76	47.7	0.58	$< 1e^{-3}$	31.7	96.9
		270	119.9	30.4	18	24	64	58.1	0.68	$< 1e^{-3}$	32.1	99.3
		450	**203.9**	**29.2**	**12**	**18**	**52**	**71.1**	**0.73**	$< 1e^{-3}$	**36.1**	**100.0**
150% increased	1.0	72	35.0	25.4	44	50	116	36.2	0.11	$6.3e^{-1}$	66.8	61.4
		180	81.3	29.4	24	30	76	68.1	0.43	$1.9e^{-2}$	39.0	86.1
		270	119.9	30.4	18	24	64	83.0	0.60	$< 1e^{-3}$	29.4	94.2
		450	**203.9**	**29.2**	**12**	**18**	**52**	**101.6**	**0.74**	$< 1e^{-3}$	**25.8**	**98.6**
	1.3	72	40.1	19.4	40	46	108	40.9	0.23	$2.5e^{-1}$	52.6	74.1
		180	81.3	29.4	24	30	76	68.1	0.63	$< 1e^{-3}$	28.5	96.6
		270	119.9	30.4	18	24	64	83.0	0.74	$< 1e^{-3}$	27.8	99.2
		450	**203.9**	**29.2**	**12**	**18**	**52**	**101.6**	**0.79**	$< 1e^{-3}$	**31.3**	**100.0**
	1.5	72	35.0	25.4	44	50	116	36.2	0.33	$8.5e^{-2}$	44.7	82.3
		180	81.3	29.4	24	30	76	68.1	0.70	$< 1e^{-3}$	28.8	98.8
		270	119.9	30.4	18	24	64	83.0	0.77	$< 1e^{-3}$	31.1	99.8
		450	**190.8**	**33.4**	**12**	**20**	**54**	**98.2**	**0.79**	$< 1e^{-3}$	**35.6**	**100.0**

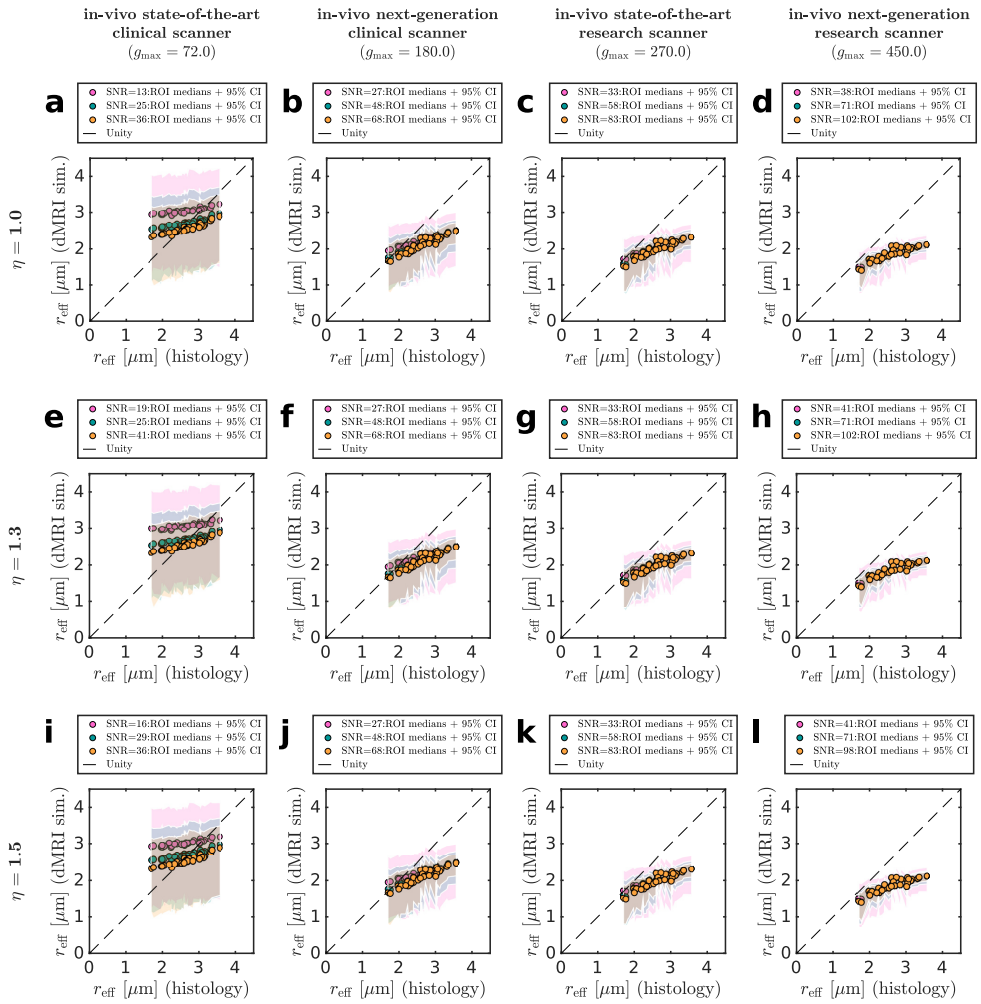

Fig. S8 Estimated r_{eff} from optimal in-vivo dMRI protocols. The plots show r_{eff} derived from dMRI simulations with optimal protocols against the histological r_{eff} for various maximum gradient amplitudes g_{max} of existing/upcoming scanners (columns), assuming 90 % of nominal values. The η values (rows) denote radius scaling factors compensating for tissue shrinkage in histology data. While $\eta = 1.3$ reflects the value assumed in the main manuscript, $\eta = 1$ and $\eta = 1.5$ reflect more extreme cases of no tissue shrinkage or very strong tissue shrinkage. Markers represent histological ROIs in Fig. 1a. The 95 % confidence interval for ROIs (shaded areas) was computed across 1000 noise realizations. Colors indicate different SNR baseline levels. While the reference SNR baseline level reflects our experimental conditions, increased SNR baseline levels assume an SNR increase through potential technical or acquisition advances. In addition, the SNR of a particular protocol candidate depends on the protocol parameters (see Eq. (13)). See Table S1 for the full set of protocol parameters and metrics for protocols shown here.

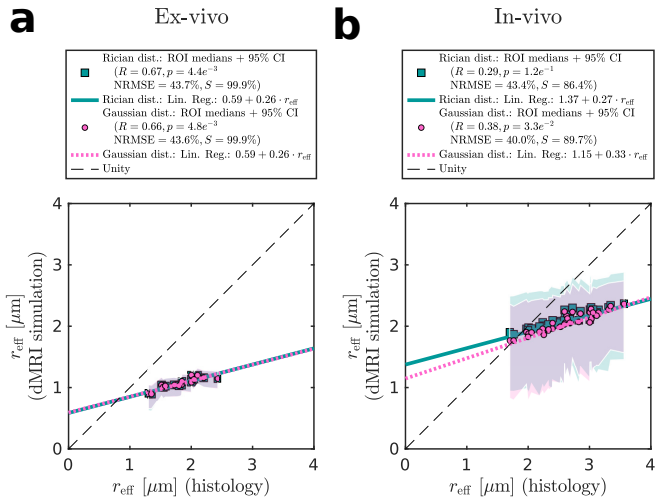

Fig. S9 Influence of Gaussian and Rician noise on r_{eff} estimation. Comparison of r_{eff} from dMRI simulations against histological values for our experimental **(a)** ex-vivo and **(a)** in-vivo dMRI protocols. Results are shown for both Gaussian and Rician noise (see legend). Markers represent histological ROIs in Fig. 1a. The 95 % confidence intervals (shaded areas) were computed across 1000 noise realizations. The dashed lines illustrate theoretical perfect agreement. The legends provide metrics computed over all ROIs, including Pearson's correlation coefficient (R) and the corresponding p-value, the normalized root-mean-square error (NRMSE), and the fitting success rate (S) (see Section 4.7 for metric definitions).

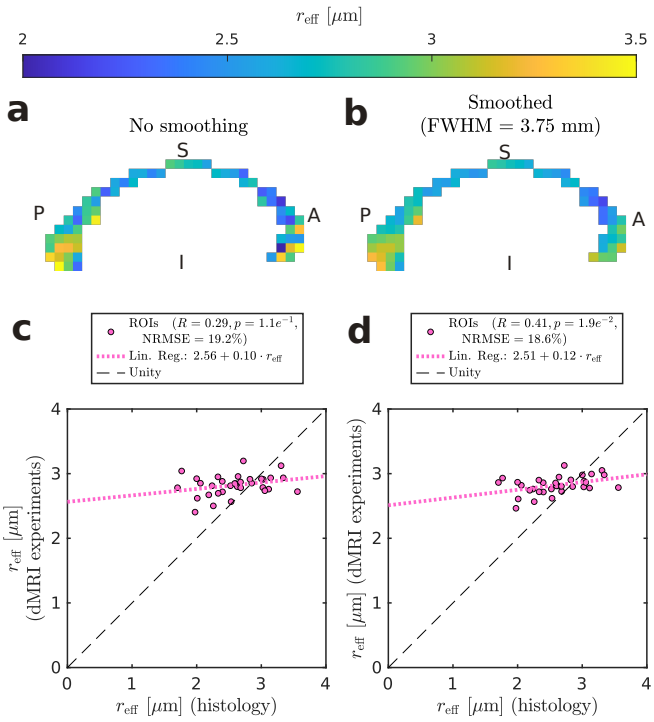

Fig. S10 Impact of spatial smoothing on in-vivo dMRI-based r_{eff}. **(a-b)** Spatial patterns of r_{eff} across the corpus callosum: **(a)** before smoothing and **(b)** after smoothing with FWHM = 3.75 mm (1.5× voxel size). Patterns show mid-sagittal section of the corpus callosum for an exemplary subject in native space. **(c-d)** Quantitative comparison of in-vivo dMRI-based group-average r_{eff} against histology. The group-average r_{eff} was computed from different per-subject maps: **(c)** from unsmoothed maps, as illustrated in (a), and **(d)** from smoothed maps, as illustrated in (b). Markers represent histological ROIs in Fig. 1a. The dashed lines illustrate theoretical perfect agreement. The legends provide metrics computed over all ROIs, including Pearson's correlation coefficient (R) and the corresponding p-value, the normalized root-mean-square error (NRMSE) (see Section 4.7 for metric definitions).